Dalton Transactions

ROYAL SOCIETY OF CHEMISTRY

PAPER

View Article Online
View Journal | View Issue

Cite this: *Dalton Trans.*, 2026, **55**, 6480

Single-crystalline ordered mesoporous indium tin oxides with controlled Sn/In ratio *via* vapor-phase oxidation of metal chlorides within silica colloidal crystals

Tomohiro Okita,[a] Ryoma Uchida,[a] Atsushi Shimojima [a,b,c] and Takamichi Matsuno *†[a,b,c]

Received 19th December 2025,
Accepted 26th March 2026

DOI: 10.1039/d5dt03043a

rsc.li/dalton

The properties of nanoporous metal oxides depend on their pore structure and the internal structure of the pore walls, and precise control of such factors is crucial. In particular, single-crystalline nanoporous metal oxides, in which the pore walls consist of a single crystal, exhibit characteristics of both single crystals and nanoporous materials that are distinct from conventional polycrystalline materials. Herein, we report the synthesis of single-crystalline mesoporous indium tin oxide (ITO) with a pore diameter of ~30 nm and a controlled Sn/In ratio. The synthesis was achieved using regularly arranged silica nanospheres (silica colloidal crystals) as a template, followed by crystal growth of ITO within the template by oxidation of metal chloride precursors. By increasing the oxygen-to-metal chloride ratio, crystal growth outside the template was suppressed and the volatilization of Sn species was reduced, thereby enabling an increase in the Sn/In molar ratio to 0.10, which is critical for electrical conductivity.

Introduction

Nanoporous metal oxides exhibit the functionalities of metal oxides, such as electronic and ionic conductivity, catalytic activity, and magnetism, alongside characteristics derived from nanoporous structures, including high specific surface area and large pore volume. Due to these characteristics, nanoporous metal oxides are applicable across a wide range of fields, including energy conversion, catalysis, photocatalysis, and electronic devices.[1,2] In particular, single-crystalline nanoporous metal oxides, in which the pore wall is composed of a single crystallite, have garnered attention for their superior properties compared to typical nanoporous metal oxides composed of nanocrystals. For example, enhanced electronic and ionic conductivity[3] and reduced recombination centers[4] have been reported. Synthesis methods for nanoporous metal oxides include the soft-templating method,[5,6] which uses surfactant or block copolymer micelles as templates, the hard-templating method,[1,7] which employs inorganic nanoporous materials or nanoparticles as templates, and methods utilizing volume shrinkage during the pyrolysis or oxidation of single crystals.[8,9] Among these, the hard-templating method is particularly useful because it employs rigid, thermally stable inorganic materials as templates, enabling precise control of the porous structure and suppressing template collapse during crystal growth.

As synthetic methods for growing metal oxide crystals inside templates, calcination of low-melting-point metal salts[10,11] and solvothermal processes[12–18] have been widely developed. In the calcination process, the precursor infiltrated into the template melts and decomposes upon heating, allowing nucleation and crystal growth to proceed within the molten salt. However, this method requires selecting precursors with melting points lower than the decomposition temperature. Furthermore, controlling nucleation and crystal growth through decomposition and combustion during high-temperature calcination is difficult, making it unsuitable for many metal oxides. In contrast, the solvothermal method, in which a template is immersed in a precursor solution and heated under high pressure, causes nucleation and crystal growth of metal oxides within the liquid phase. The continuous supply of the precursor in solution yields metal oxide single crystals with relatively large crystal sizes. However, controlling selective nucleation and growth within the template is

[a]*Department of Applied Chemistry, Faculty of Science and Engineering, Waseda University, 3-4-1 Okubo, Shinjuku-ku, Tokyo 169-8555, Japan.*
E-mail: matsuno@aoni.waseda.jp
[b]*Waseda Research Institute for Science and Engineering, Waseda University, 3-4-1 Okubo, Shinjuku-ku, Tokyo 169-8555, Japan*
[c]*Kagami Memorial Research Institute for Materials Science and Technology, Waseda University, 2-8-26 Nishiwaseda, Shinjuku-ku, Tokyo 169-0051, Japan*
† Present address: Waseda Institute for Advanced Study, Waseda University, 1-21-1 Nishiwaseda, Shinjuku-ku, Tokyo 169-0051, Japan.

difficult. Furthermore, hydroxides and/or oxyhydroxides may be formed instead of the desired oxide. For these reasons, previous reports on single-crystalline nanoporous oxides synthesized by the solvothermal method are limited to certain oxides, such as SnO_2,[12,13] TiO_2,[12,14,15] CeO_2,[12] $BiVO_4$,[16] and zeolites.[17,18] In addition to the above two methods, a technique using mineralizers to crystallize metal oxides at relatively low temperatures[19] has also been reported, but it is limited to synthesizing quartz.[20,21] Therefore, developing a method to realize single-crystalline nanoporous metal oxides for compounds that were previously difficult to synthesize, while controlling the nucleation and crystal growth processes, is an important challenge.

Recently, we discovered that single-crystalline nanoporous metal oxides with an inverse opal structure[22] can be synthesized by a chemical-vapor-based confined crystal growth (C^3) method, in which metal chlorides are heated and oxidized within the interparticle nanopores of silica colloidal crystals (SCCs) used as a template.[23,24] The metal chloride volatilizes upon heating and undergoes oxidation while diffusing in the gas phase within the template. This process is considered to continuously supply the precursor to the metal oxide nucleus, enabling crystal growth. Because the metal chlorides themselves do not undergo thermal decomposition upon heating, nucleation and crystal growth are more controllable compared to the conventional calcination process. In the α-Fe_2O_3 system, it has been shown that crystallite size can potentially be tuned by varying the oxygen supply.[23]

A previous report demonstrated the synthesis of single-crystalline nanoporous indium tin oxides (ITOs), using SCCs as templates and indium chloride and tin chloride as precursors, and investigated their thermoelectric conversion performance.[24] A decrease in thermal conductivity is important to improve the performance, and introducing a nanoporous structure is an effective way. However, in conventional approaches, the numerous grain boundaries in the pore walls caused an unintended decrease in electrical conductivity. In contrast, single-crystalline nanoporous ITOs could significantly reduce thermal conductivity while suppressing an unintended decrease in electrical conductivity by minimizing grain boundaries in the pore walls. Although clarifying the correlation between the porous structure and thermal and electrical conductivities is important, the previous study had limitations in controlling pore size, with the smallest pore size being 39 nm. This was due to a problem where part of the volatilized precursor diffused and precipitated outside the template, forming nonporous crystals. In particular, reducing the size of the silica nanospheres constituting SCCs to 28 nm led to crystallization primarily outside the template, and the synthesis of mesoporous ITOs was difficult. This is presumably due to the small pore size of the template, which slows down air diffusion into its interior. In addition, the Sn/In molar ratio, crucial for electrical conductivity, was lower than the target value of 0.10.[25] The relatively high vapor pressure of $SnCl_4$[26,27] likely caused faster volatilization than $InCl_3$, leading to diffusion out of the template and a reduction in the doping amount.

In this study, to synthesize single-crystalline mesoporous ITO with a controlled composition, we increased the oxygen-to-metal chloride ratio within the SCCs by increasing the air volume in the calcination vessel and reducing the amount of metal chlorides infiltrated into the SCCs, thereby suppressing crystal growth outside the template while increasing the Sn/In ratio (Scheme 1). As a result, ITO was selectively crystallized within the SCCs composed of 29–30 nm silica nanospheres, successfully achieving the Sn/In ratio of 0.10. Furthermore, it was found that the crystallite size of the mesoporous ITOs varies with the oxygen-to-metal chloride ratio.

Experimental

Materials

Tris(hydroxymethyl)aminomethane (THAM, >99.0%), tetraethoxysilane (TEOS, >99.0%), indium(III) chloride tetrahydrate ($InCl_3{\cdot}4H_2O$, >99.9%), and potassium hydroxide (>85.0%) were purchased from Fujifilm Wako Pure Chemical Corp. Tin(IV) chloride pentahydrate ($SnCl_4{\cdot}5H_2O$, >98.0%) was purchased from Fujifilm Wako Pure Chemical Corp. and Sigma-Aldrich. All reagents were used as received.

Synthetic procedures

Preparation of silica colloidal crystals. Silica colloidal crystals (SCCs) were prepared as templates for mesoporous ITOs, following the previous reports.[28,29] A silica nanosphere dispersion was prepared as follows. THAM (9.68 g) was dissolved in pure water (400 mL) and stirred at 80 °C for 1 h in a 1 L recovery flask. TEOS (321 mL) was added to the solution, and the mixture was stirred at 80 °C for 24 h, yielding a silica nanosphere dispersion (molar ratio was 90 TEOS : 1390 H_2O : 5 THAM). The average diameter of the silica nanospheres slightly varied between batches, and the values were 29 nm (coefficient of variation (CV): 5.5%) and 30 nm (CV: 6.7%). The mean diameter and coefficient of variation were calculated by measuring the diameters of 100 silica nanospheres from transmission electron microscopy (TEM) images. The silica nanosphere dispersion was dried at 40 °C, then calcined at 600 °C for 6 h to remove THAM (heating and cooling rate: 1.7 °C min^{-1}), yielding SCCs composed of silica nanospheres with diameters of 29 nm or 30 nm. The samples are denoted as SCCs-29 and SCCs-30, respectively.

Synthesis of single-crystalline mesoporous ITO under increased air volume. Mesoporous ITOs were synthesized using SCCs as a template (Scheme 1b-i). SCCs were heated at 150 °C for 3 h to remove adsorbed water before use. An ITO precursor was prepared by stirring a mixture of pure water (0.9 mL), $InCl_3{\cdot}4H_2O$ (240 mg, 0.83 M), and $SnCl_4{\cdot}5H_2O$ (28 mg, 0.083 M) at room temperature for 10 min (Sn/In molar ratio: 0.10). The ITO precursor was then infiltrated into the interparticle pores of the dried SCCs (1.8 g) and left in a desiccator with silica gel for 3 days to dry. The infiltration process was divided into five times, with at least 7 h in the desiccator

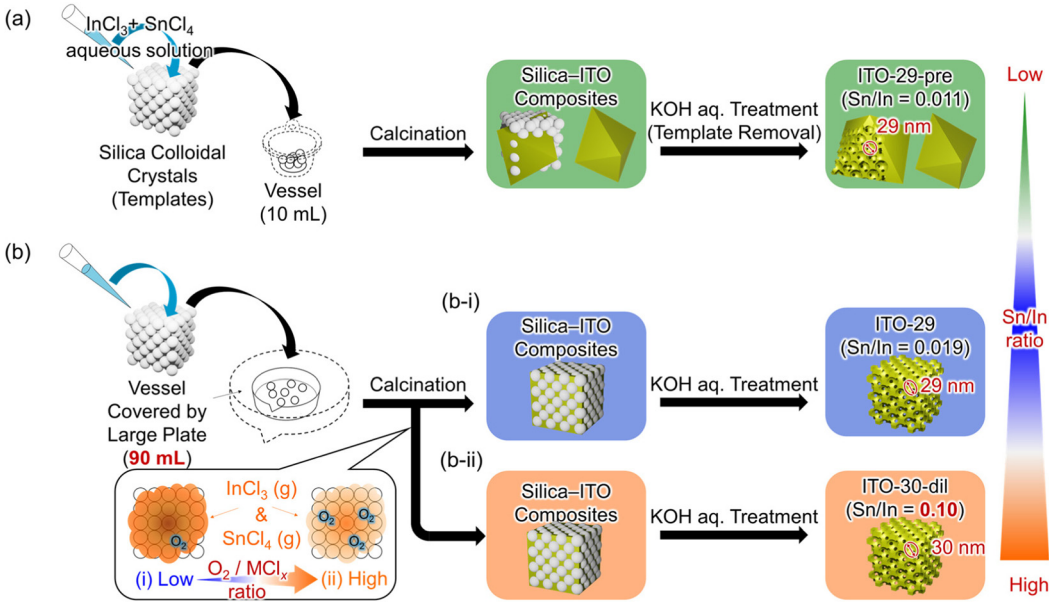

Scheme 1 Synthesis of single-crystalline ordered mesoporous ITOs with controlled Sn/In ratio by crystal growth inside silica colloidal crystals under different oxygen amount conditions. (a) Calcination in a 10 mL vessel (previous condition) and (b) calcination in a 90 mL vessel with (i) the same precursor concentration as (a) and (ii) a diluted precursor concentration.

between each addition of precursor solution. The volume of the precipitated hydrated metal chlorides was adjusted to occupy 20% of the pore volume. Subsequently, the sample was calcined in air to crystallize ITO within the SCCs. After heating at 300 °C for 2 h, the temperature was raised to 450 °C and kept for 5 h (heating and cooling rate: 1.0 °C min^{-1}). To suppress ITO precursor leakage outside the template by volatilization, the vessel volume was changed from 10 mL to 90 mL to increase the amount of air compared to the previously reported conditions.[24] Then, the sample was added to 500 mL of 2 M KOH aq. and stirred at 60 °C for 24 h to remove the template. After filtering the solution, the solid sample was washed with pure water and ethanol. These procedures were repeated twice to complete template removal. The resulting sample was dried at 80 °C for 24 h in an oven, yielding a yellow-green colored powder. Hereafter, this sample is denoted as ITO-29 (the number indicates silica nanosphere diameter). As a comparative sample, a mesoporous ITO was also synthesized under the conditions of the previous study,[24] in which crystal growth occurred outside the template (Scheme 1a). The sample was obtained *via* calcination in a 10 mL crucible at 450 °C for 5 h (heating and cooling rate: 1.0 °C min^{-1}). This sample is denoted as ITO-29-pre.

Synthesis of single-crystalline mesoporous ITO with a higher In/Sn ratio. The Sn/In molar ratio and the concentration of the precursor were investigated to increase the Sn/In ratio in the sample. The samples were prepared using precursor solutions with a Sn/In ratio of 0.20 by the same procedure as ITO-29: one at the same precursor concentration as ITO-29, and another diluted to one-tenth (Scheme 1b-ii). The samples are denoted as ITO-30-0.2 and ITO-30-0.2-dil, respectively.

Characterization

Scanning electron microscopy (SEM) images were obtained using a Hitachi S-5500 electron microscope operating at 1.0–5.0 kV. The TEM images were also obtained using a JEOL JEM-2010 electron microscope operating at 200 kV. TEM and SEM samples were prepared as follows: an ethanol suspension of the powder sample was drop-cast onto a carbon-coated Cu microgrid and vacuum-dried. The SEM sample was prepared by sticking a small amount of the powder sample to a piece of carbon tape. Powder X-ray diffraction (XRD) measurements were carried out on Rigaku RINT-Ultima III with a parallel beam geometry, equipped with a scintillation detector and a parabolic multilayer mirror. The RINT Ultima III diffractometer was operated with Cu Kα radiation at 40 kV and 40 mA. Small-angle X-ray scattering (SAXS) patterns were measured on a Rigaku NANO-Viewer using Cu Kα radiation operating at 40 kV and 30 mA and a Dectris PILATUS 2D X-ray detector. N_2 adsorption–desorption measurements were conducted by Quantachrome Autosorb-iQ. The sample was pretreated by heating at 120 °C for 4.5 h under vacuum and then measured at −196 °C. The specific surface area was calculated by the Brunauer–Emmett–Teller (BET) method,[30] and the pore diameter distribution was calculated by the Barrett–Joyner–Halenda (BJH) method.[31] X-ray photoelectron spectroscopy (XPS) was conducted using an Ulvac-PHI VersaProbe II. A monochromatized Al Kα line was used, and the pass energy was 23.5 eV. Inductively coupled plasma optical emission spectrometry (ICP-OES) was performed using an Agilent Technologies Agilent 5100 SVDV. The mesoporous ITO sample was dissolved in the mixture of 5 mL HCl aq. (35%), HNO_3 aq.

(61%), and HF aq. (48%) by 20 min microwave treatment at 230 °C in a Teflon-lined vessel for measurements.

Results and discussion

First, ITO-29 and ITO-29-pre, which were synthesized by varying the amount of air during calcination, are compared. Then, the results for ITO-30-0.2 and ITO-30-0.2-dil, which varied the composition and concentration of the precursor solution, are discussed. SCCs composed of regularly arranged silica nanospheres in a face-centered cubic (fcc) structure were confirmed based on the SEM and TEM images, N_2 adsorption–desorption isotherms (Fig. S1, SI), and SAXS patterns (Fig. S2, SI). These results were consistent with those reported in the previous study.[32] The XRD patterns of the ITO-29 and ITO-29-pre (Fig. 1) show peaks corresponding to cubic In_2O_3, along with minor peaks corresponding to rhombohedral In_2O_3, and no peaks derived from SnO_2 were observed. Some reports suggest that doping In_2O_3 with heteroatoms distorts the crystal lattice, leading to the formation of the rhombohedral phase.[33–35] Similarly, in ITO-29, rhombohedral phase formation is possibly due to the distortion of the In_2O_3 crystal lattice by Sn doping. XPS spectra (Fig. S3, SI) revealed peaks corresponding to Sn $3d_{3/2}$ and Sn $3d_{5/2}$ [36] at 495.1 eV and 486.6 eV, respectively. The peaks corresponding to In $3d_{3/2}$ and In $3d_{5/2}$ [36] were also observed at 451.6 eV and 444.2 eV. The In peaks were asymmetric, and curve fitting confirmed the presence of peaks derived from Sn–O–In.[37] These results indicate the formation of Sn-doped indium oxides.

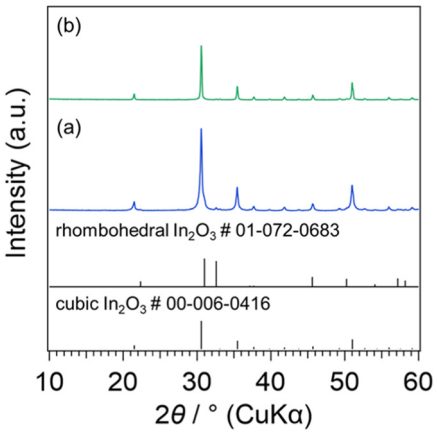

Fig. 1 XRD patterns of (a) ITO-29 and (b) ITO-29-pre. The simulated patterns of In_2O_3 based on ICDD data are shown at the bottom.

The Sn/In ratio calculated from ICP-OES results was 0.019 for ITO-29 and 0.011 for ITO-29-pre, both lower than the composition ratio of the ITO precursor solution (0.10). This is considered to occur because $SnCl_4$ has a higher vapor pressure than $InCl_3$ [26,27] (Fig. S4, SI), making it easier for $SnCl_4$ to diffuse to the outside of the template before oxidation upon heating. This explanation is consistent with the result that the Sn/In ratio was lower for ITO-29-pre synthesized under conditions with less air.

SEM and TEM images (Fig. 2a–c) revealed mesoporous particles with regularly arranged spherical pores in ITO-29. The FFT pattern of the TEM image (Fig. 2d) showed regular spots corresponding to fcc [100], confirming the replication of the template's pore structure. The average pore diameter measured from TEM images was 28 nm (CV: 3.7%), almost consistent with the size of silica nanospheres. The SAED patterns measured in regions of several hundred nm in size (Fig. 2e) showed spots indicative of single-crystallinity. In many views, SAED patterns were slightly elongated in an arc shape, as represented in Fig. 2e, suggesting that the crystal orientations were not completely aligned in the same direction and that the pore walls of the mesoporous particles were distorted. Furthermore, some fields of view showed spots originating from multiple crystals, suggesting that two or more crystals

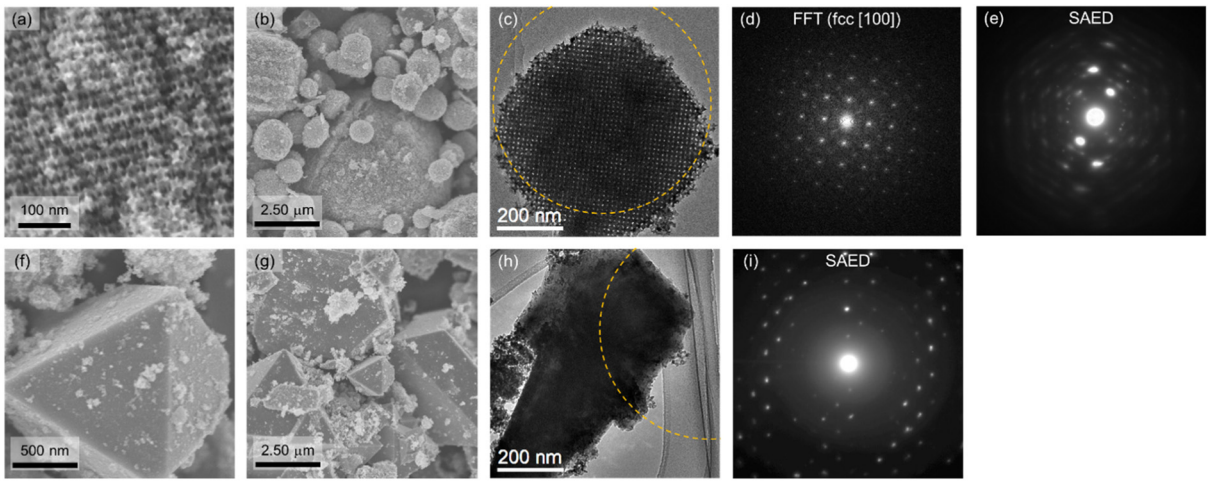

Fig. 2 (a and b) SEM images, (c) TEM image, (d) FFT pattern, and (e) SAED pattern corresponding to the orange circle in (c) of ITO-29 and (f and g) SEM images, (h) TEM image, and (i) SAED pattern corresponding to the orange circle in (h) of ITO-29-pre.

may have coalesced during growth (Fig. S5, SI). Another cause is the presence of small fragments derived from mesoporous ITO on the particle (Fig. S5, SI). Based on the above results, synthesis of mesoporous ITO with an inverse opal structure composed of crystallites larger than several hundred nm was confirmed. In contrast, ITO-29-pre showed not only mesoporous structures but also non-porous particles (Fig. 2f–i), suggesting crystal growth occurred outside the template, as confirmed in the previous report.[24]

The T-SAXS patterns (Fig. S2a, SI) showed peaks attributed to an fcc structure for both samples, confirming the replication of the porous structure from the SCCs template. The center-to-center distance of the pores, calculated from the d value of the fcc 111 diffraction, was 28 nm, consistent with the average diameter of the silica nanospheres. The N_2 adsorption–desorption isotherms (Fig. 3a) of both samples were type IV(a), showing a steep uptake at around P/P_0 = 0.90. A significant difference in total adsorption capacity was observed between ITO-29 and ITO-29-pre. The BJH pore diameter distributions (Fig. 3b) showed an intense peak at 24 nm calculated from the adsorption isotherm, indicating the formation of uniform mesopores. The pore size distribution calculated from the desorption isotherm shows a peak at 11 nm, corresponding to the size of window pores connecting spherical mesopores. The pore volume of ITO-29 was 0.32 $cm^3\ g^{-1}$, with a BET surface area of 83 $m^2\ g^{-1}$. ITO-29-pre had a pore volume of 0.078 $cm^3\ g^{-1}$ and a BET surface area of 36 $m^2\ g^{-1}$. The pore volume of ITO-29 was relatively close to the geometrically calculated value assuming an ideal fcc structure (0.40 $cm^3\ g^{-1}$) and was almost 4 times larger than that of ITO-29-pre. On a volumetric basis, ~94% of ITO-29 consists of an inverse opal structure, while ITO-29-pre consists of ~49% (see SI). In addition, the BET surface area of ITO-29 was close to the calculated value (85 $m^2\ g^{-1}$) (see SI). These results indicate that crystal growth outside the template was significantly suppressed in ITO-29, yielding a mesoporous structure closer to the ideal inverse opal structure.

Based on the above results, it was found that increasing the air volume during calcination facilitates the oxidation of metal chlorides within the template, thereby suppressing the volatilization of precursors outside the template. The sample yields were 49% for ITO-29 and 22% for ITO-29-pre, with the smaller vessel showing a lower yield. The ratio of oxygen inside the vessel to the amount required to oxidize all metal chlorides was 29% for the previously reported condition (note that a gap was present between the lid and vessel) and 265% for the condition of the present study. Therefore, the oxygen supply was insufficient under the previously reported condition. This likely caused leakage of metal chlorides from the template, resulting in the reduced yield of mesoporous ITO.

Changing the container size alone proved insufficient to suppress volatilization of the Sn species. Therefore, increasing the Sn/In ratio was attempted by increasing the precursor solution composition to Sn/In = 0.20 and reducing the amount of infiltrated precursor to one-tenth, thereby lowering the metal chloride concentration within the template. As a result, the formation of a single-crystalline mesoporous ITO with an inverse opal structure (ITO-30-0.2-dil), similar to ITO-29, was confirmed (Fig. 4 and Fig. S2, S3, and S6, SI), and the Sn/In ratio calculated from the ICP-OES result reached 0.10. The XRD pattern, N_2 adsorption–desorption isotherms, XPS spectrum, and SAXS pattern showed almost no change compared with ITO-29. Based on the TEM images (Fig. 4d and Fig. S6a and c, SI), the average pore diameter was 28 nm (CV: 3.1%), also the same as ITO-29. The SAED patterns and corresponding DF-TEM images (Fig. 4e and Fig. S6b and d) show that the mesoporous ITO is composed of multiple crystals, suggesting the coalescence of crystals during growth. It was found that the average size was ~600 nm (CV: 35.7%), which is smaller than those of ITO-29 (1.7 μm, CV: 42.7%) and ITO-29-pre (3.5 μm, CV: 76.0%). This difference would be due not to mechanical destruction, but an increase in nucleation frequency caused by a relatively higher oxygen content compared to ITO-29 and ITO-29-pre, and a decrease in crystal growth rate caused by a lower precursor concentration in the gas phase. This is consistent with the finding that no fractured nanoporous structures were observed by electron microscopy analyses for ITO-29 and ITO-30-0.2-dil.

In the ITO-30-0.2, where only the composition ratio of the precursor was changed to Sn/In = 0.20 without altering the concentration, the Sn/In ratio in the sample was 0.018. The Sn/In ratio is almost identical to that of ITO-29, indicating that even when the amount of Sn in the precursor is increased, most of the tin chloride volatilizes under conditions where sufficient oxidation does not occur. Based on the characterization of ITO-30-0.2 (Fig. S7, SI), the crystal structure and nanoporous structure of ITO-30-0.2 were almost the same as those of ITO-29.

According to the ITO-30-0.2 result, the Sn/In ratio in the precursor solution did not improve the Sn/In ratio; rather, increasing the oxygen-to-metal chloride ratio within the template by reducing the infiltration amount of the precursor solution was crucial. Although oxygen partial pressure may also influence nucleation and crystal growth, its effects remain unclear at this stage. To better understand the formation and crystal growth of metal oxides within nanopores, further

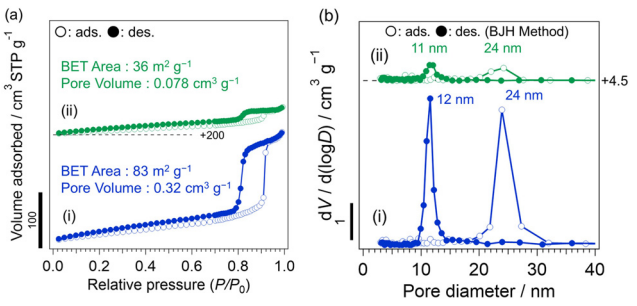

Fig. 3 (a) N_2 adsorption–desorption isotherms and (b) BJH pore diameter distributions of (i) ITO-29 and (ii) ITO-29-pre (○: adsorption, •: desorption).

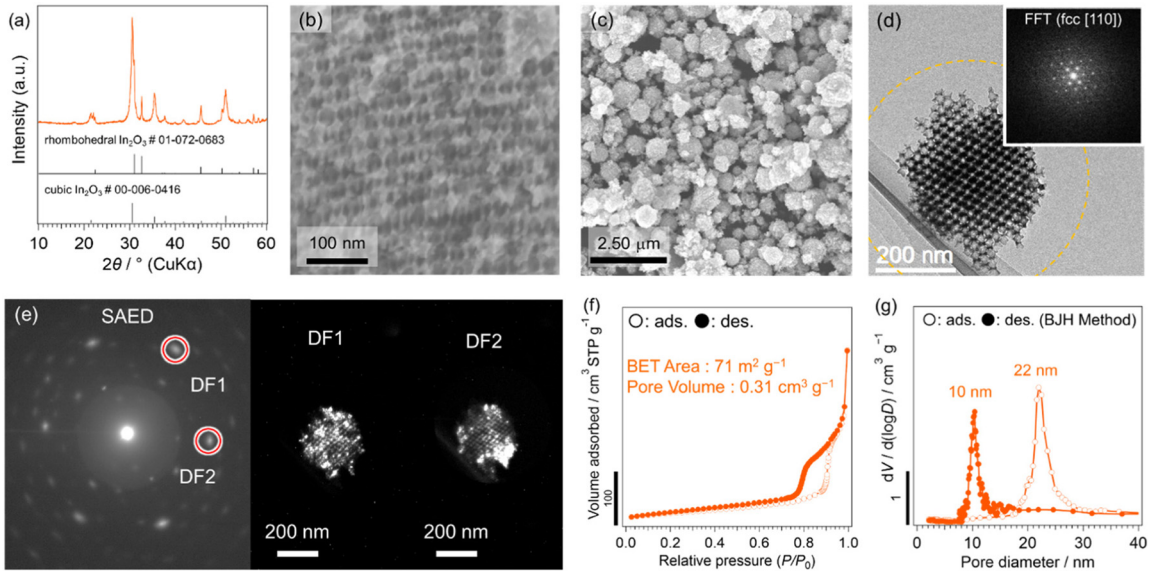

Fig. 4 (a) XRD pattern, (b and c) SEM images, (d) TEM image (inset: FFT pattern), (e) SAED pattern corresponding to the orange circle in (d) and DF-TEM images, (f) N_2 adsorption–desorption isotherms, and (g) BJH pore size distributions of ITO-30-0.2-dil (○: adsorption, •: desorption).

exploration of synthesis conditions and applicable metal oxide systems is needed.

Conclusions

Using silica colloidal crystals consisting of regularly arranged silica nanospheres with an average diameter of ~30 nm as a template, single-crystalline mesoporous indium tin oxides (ITOs) with ~30 nm spherical mesopores were successfully synthesized by crystal growth within the template induced by the volatilization and oxidation of metal chlorides within the pores. The oxygen-to-metal chloride ratio was found to be crucial for crystal growth within the template. Increasing the oxygen amount by changing the size of the calcination vessel enabled oxydation of metal chlorides within the nanopores, thereby suppressing crystal growth outside the template. Furthermore, by reducing the infiltration amount to increase the oxygen-to-metal chloride ratio, the proportion of highly volatile $SnCl_4$ that oxidized before diffusing outside of the template was increased, thereby raising the Sn/In ratio in the sample to 0.10. Simultaneously, crystal sizes decreased, indicating an increase in nucleation frequency. This result indicates that the crystallite size can be controlled depending on the oxygen-to-metal chloride ratio.

Author contributions

All authors have contributed to writing the manuscript and approved the final version of the manuscript. T. O. and T. M. designed the research. T. O. performed the experiments and analyses and wrote the manuscript under the supervision of A. S. and T. M. R. U., A. S., and T. M. provided technical and scientific support.

Conflicts of interest

There are no conflicts to declare.

Data availability

The data supporting this article have been included as part of the supplementary information (SI). Supplementary information: descriptions of the calculation for the proportion of porous material formation in mesoporous ITOs and geometrical calculation for the BET areas and pore volumes of mesoporous ITOs, vapor pressure–temperature curves, SAXS patterns, N_2 adsorption–desorption isotherms, TEM images, SEM images, XPS spectra, and a XRD pattern. See DOI: https://doi.org/10.1039/d5dt03043a.

Acknowledgements

The authors thank Dr Noriko Hanzawa and Mr Toshiyuki Akanuma (Waseda University) for TEM observation, Mr Takahiro Gotoh (Waseda University) for XPS analysis, Mr Takeshi Mino (Waseda University) for SAXS analysis, Ms Hiromi Aoki and Dr Ryota Takahashi (Waseda University) for ICP-OES analysis, Dr Takuya Hikino, Mr Takaaki Nakano, Mr Daichi Oka, Mr Toshihide Miyake, Mr Hideaki Basyomatsu, Mr Takeshi Iwakami, Ms Momoka Ito, Ms Mayu Suzuki, Mr Tomonori Suga, Mr Kazuki Hondo, and Ms Fran Ama (Waseda University) for their valuable support with the measurements

and discussions. This work was supported by a JST FOREST Program (Grant Number JPMJFR2224), a Grant-in-Aid for Early-Career Scientists (Grant Number JP22K14481), and a 2025 research grant from Amano Institute of Technology. This work was the result of using research equipment (Ulvac-PHI VersaProbe II (C1051), Agilent Technologies Agilent 5100 SVDV (D1001), Rigaku NANO-Viewer (G1008), Hitachi S-5500 (G1028), JEOL JEM-2010 (G1024), Rigaku RINT-Ultima III (G1035), Quantachrome Autosorb-iQ (G1038)) shared in the MEXT Project for promoting public utilization of advanced research infrastructure (program for supporting construction of core facilities) Grant Number JPMXS0440500025.

References

1 Y. Ren, Z. Ma and P. G. Bruce, *Chem. Soc. Rev.*, 2012, **41**, 4909.
2 S. L. Suib, *Chem. Rec.*, 2017, **17**, 1169.
3 X. Jin, Y. Han, Z. Zhang, Y. Chen, J. Li, T. Yang, X. Wang, W. Li, X. Han, Z. Wang, X. Liu, H. Jiao, X. Ke, M. Sui, R. Cao, G. Zhang, Y. Tang, P. Yan and S. Jiao, *Adv. Mater.*, 2022, **34**, 2109356.
4 W. Li and K. Xie, *Acc. Chem. Res.*, 2023, **56**, 374.
5 M. C. Orilalla and U. Wiesner, *Chem. Soc. Rev.*, 2011, **40**, 520.
6 L. Duan, C. Wang, W. Zhang, B. Ma, Y. Deng, W. Li and D. Zhao, *Chem. Rev.*, 2021, **121**, 14349.
7 X. Deng, K. Chen and H. Tüysüz, *Chem. Mater.*, 2017, **29**, 40.
8 Y. Xiao and K. Xie, *Angew. Chem., Int. Ed.*, 2022, **61**, e202113079.
9 S.-Z. Huang, J. Jin, Y. Cai, Y. Li, Z. Deng, J.-Y. Zeng, J. Liu, C. Wang, T. Hasan and B. L. Su, *Sci. Rep.*, 2015, **5**, 14686.
10 K. Jiao, B. Zhang, B. Yue, Y. Ren, S. Liu, S. Yan, C. Dickinson, W. Zhou and H. He, *Chem. Commun.*, 2005, **45**, 5618.
11 W. Yue and W. Zhou, *Chem. Mater.*, 2007, **19**, 2359.
12 X. Zheng, Y. Lv, Q. Kuang, Z. Zhu, X. Long and S. Yang, *Chem. Mater.*, 2014, **26**, 5700.
13 S. Xiao, L. Wang, Z. Qin, X. Chen, L. Chen, Y. Li and K. Shen, *ACS Cent. Sci.*, 2024, **10**, 374.
14 E. J. W. Crossland, N. Nobel, V. Sivaram, T. Leijtens, J. A. Alexander-Webber and H. J. Snaith, *Nature*, 2013, **495**, 215.
15 W. Yue, X. Xu, J. T. S. Irvine, P. S. Attidekou, C. Liu, H. He, D. Zhao and W. Zhou, *Chem. Mater.*, 2009, **21**, 2540.
16 J. Niu, J. Albero, P. Atienzar and H. Garia, *Adv. Funct. Mater.*, 2020, **30**, 1908984.
17 L.-H. Chen, M.-H. Sun, Z. Wang, W. Yang, Z. Xie and B.-L. Su, *Chem. Rev.*, 2020, **120**, 11194.
18 K. Takaoka, T. Matsuno, M. Koike, N. Muramoto, H. Wada, K. Kuroda and A. Shimojima, *Small*, 2025, **21**, 2405280.
19 L. Lermusiaux, A. Mazel, A. Carretero-Genevrier, C. Sanchez and G. L. Drisko, *Acc. Chem. Res.*, 2022, **55**, 171.
20 A. Carretero-Genevrier, M. Gich, L. Picas, J. Gàzquez, G. L. Drisko, C. Boissiere, D. Grosso, J. Rodriguez-Carvajal and C. Sanchez, *Science*, 2013, **340**, 827.
21 T. Matsuno, Y. Kuroda, M. Kitahara, A. Shimojima, H. Wada and K. Kuroda, *Angew. Chem., Int. Ed.*, 2016, **55**, 6008.
22 A. Stein, *Langmuir*, 2023, **39**, 2890.
23 D. Oka, K. Takaoka, A. Shimojima and T. Matsuno, *Chem. Mater.*, 2025, **37**, 5005.
24 Y. Saito, T. Matsuno, Q. Guo, T. Mori, M. Kashiwagi, A. Shimojima, H. Wada and K. Kuroda, *ACS Appl. Mater. Interfaces*, 2021, **13**, 15373.
25 H. Köstlin, R. Jost and W. Rems, *Phys. Status Solidi A*, 1975, **29**, 87.
26 R. Chanson, S. Bouchoule, C. Cardinaud, C. Petit-Etienne, E. Cambril, A. Rhallabi, S. Guilet and E. Blanquet, *J. Vac. Sci. Technol., B:Nanotechnol. Microelectron.:Mater., Process., Meas., Phenom.*, 2014, **32**, 011219.
27 D. R. Stull, *Ind. Eng. Chem.*, 1947, **39**, 517.
28 K.-M. Choi and K. Kuroda, *Chem. Commun.*, 2011, **39**, 10933.
29 N. Muramoto, T. Matsuno, H. Wada, K. Kuroda and A. Shimojima, *Chem. Lett.*, 2021, **50**, 1038.
30 S. Brunauer, P. H. Emmett and E. Teller, *J. Am. Chem. Soc.*, 1938, **60**, 309.
31 E. P. Barrett, L. G. Joyner and P. P. Halenda, *J. Am. Chem. Soc.*, 1951, **73**, 373.
32 T. Matsuno, T. Nakaya, Y. Kuroda, H. Wada, A. Shimojima and K. Kuroda, *Chem. – Asian J.*, 2021, **16**, 207.
33 S. C. S. Lemos, E. Nossol, J. L. Ferrari, E. O. Gomes, J. Andres, L. Gracia, I. Sorribes and R. C. Lima, *Inorg. Chem.*, 2019, **58**, 11738.
34 L. Song, K. Dou, R. Wang, P. Leng, L. Luo, Y. Xi, C.-C. Kaun, N. Han, F. Wang and Y. Chen, *ACS Appl. Mater. Interfaces*, 2020, **12**, 1270.
35 P. Li, H. Fan, Y. Cai, M. Xu, C. Long, M. Li, S. Lei and X. Zou, *RSC Adv.*, 2014, **4**, 15161.
36 S. M. A. Durrani, E. E. Khawaja, J. Shirokoff, M. A. Daous, G. D. Khattak, M. A. Salim and M. S. Hussain, *Sol. Energy Mater. Sol. Cells*, 1996, **44**, 37.
37 P. K. Biswas, A. De, L. K. Dua and L. Chkoda, *Bull. Mater. Sci.*, 2006, **29**, 323.

